

Defining the Operational Envelope for Air Flows in the miniature Arc-jet Research Chamber (mARC II)

Jocelino Rodrigues*

NASA Postdoctoral Program at NASA Ames Research Center, Moffett Field, California, 94035, USA

Megan E. MacDonald[†], Magnus A. Haw[‡], Ramon Martinez[§], and Daniel Philippidis[¶]
NASA Ames Research Center, Moffett Field, California, 94035, USA

Sebastian Colom^{||}

AMA Inc. at NASA Ames Research Center, Moffett Field, California, 94035, USA

Ryan Chung** and Joe Hartman^{††}

Sierra Lobo Inc. at NASA Ames Research Center, Moffett Field, California, 94035, USA

The second-generation 30 kW miniature Arc-jet Research Chamber (mARC II) at NASA Ames Research Center produces high enthalpy flows relevant for entry systems ground testing. The mARC II facility has recently undergone upgrades, including the installation of a new vacuum system to address the issues preventing it from maintaining underexpanded flow under test conditions. In this work, we present data obtained from an Integrated Systems Testing campaign and provide an initial assessment of arc-jet performance following the upgrades. Air is used as the working gas for the standard mARC II arc-heater configuration with two constrictor disks. Seven runs were investigated for five test conditions to assess the lowest achievable stagnation point heat fluxes for air flow rates of 0.15 or 0.25 g s⁻¹. The heat flux was measured using a water-cooled Gardon gauge (∅4.76 mm, 3/16" hemispherical) at 70 mm from the nozzle exit plane. The new vacuum system produced test box pressures in the medium (fine) vacuum range (~0.03 torr, 4 Pa) prior to gas addition and successfully maintained underexpanded flow after gas addition. The upgrade yielded a ~4X reduction in heat flux relative to the previous system for the same set test conditions. We report the lowest heat fluxes measured in mARC II to date, ranging from 26 to 81 W cm⁻², for sonic flow enthalpies of 4–14 MJ kg⁻¹. Bulk enthalpies estimated using an energy balance method (EB²) are reported for the first time using mARC II. Initial data suggests EB² generally estimates lower enthalpies than sonic flow methods for mARC II. Lastly, laminar axisymmetric Navier–Stokes simulations were performed using the NASA DPLR code. Numerical heat flux results show good agreement with experiments at low arc powers (3–15% difference at the minimum set arc current), but discrepancy increases with arc power (49% difference at the maximum set arc current).

Nomenclature

Acronyms

CFD = Computational Fluid Dynamics
HX = Heat Exchanger
mARC I = miniature Arc-jet Research Chamber (first-generation)

*NPP Research Fellow, Thermophysics Facilities Branch, Entry Systems & Technology Division, NASA Ames Research Center.

[†] Aerospace Engineer, Thermophysics Facilities Branch, Entry Systems & Technology Division, NASA Ames Research Center.

[‡] Plasma Physicist, Thermal Protection Materials Branch, Entry Systems & Technology Division, NASA Ames Research Center.

[§] EAST and mARC Facilities Manager, Thermophysics Facilities Branch, Entry Systems & Technology Division, NASA Ames Research Center.

[¶] Aerospace Engineer, Thermophysics Facilities Branch, Entry Systems & Technology Division, NASA Ames Research Center.

^{||} Research Engineer, Thermal Protection Materials Branch, Entry Systems & Technology Division, NASA Ames Research Center.

** Test Engineer, Thermophysics Facilities Branch, Entry Systems & Technology Division, NASA Ames Research Center.

^{††} Senior Engineering Consultant, Thermophysics Facilities Branch, Entry Systems & Technology Division, NASA Ames Research Center.

mARC II	=	miniature Arc-jet Research Chamber (second-generation)
NASA	=	National Aeronautics and Space Administration
TPS	=	Thermal Protection System
TSF	=	Thermophysics Facilities Branch

Greek symbols

δ	=	percentage difference
Δ	=	change in value
η	=	arc-jet efficiency
σ	=	sonic flow parameter or standard deviation

Roman symbols

A	=	cross-sectional area
c_p	=	isobaric specific heat capacity
f	=	frequency
h	=	enthalpy
I_{arc}	=	arc current
\dot{m}	=	mass flow rate
p	=	pressure
P	=	power
\dot{q}	=	heat flux
t	=	time
T	=	temperature
V_{arc}	=	arc voltage
x_i	=	axial distance from the nozzle exit plane to the instrumentation measurement plane

Superscripts

$(\bar{\cdot})$	=	average or bulk value
-----------------	---	-----------------------

I. Introduction

THE success of NASA's diverse space exploration portfolio hinges heavily on the success of a pivotal mission phase called *atmospheric entry*. The survival of spacecraft through the harsh conditions endured during entry is undeniably tied to the development of innovative materials, thermal protection systems, and instrumentation technologies. This innovation cycle requires extensive ground testing under the predicted aerothermal conditions [1]. Ground test facilities (e.g., impulse tunnels, ballistic ranges, and arc-jets) are dedicated to the study of atmospheric entry phenomena at a range of different enthalpy conditions, whereby each facility type provides valuable insights into different key aerothermal elements of the atmospheric entry phase [2].

Over the past 60 years, NASA has established a strong legacy in ground testing, including arc-jet testing [3–8]. The significance of arc-jets cannot be overstated, as they have been consistently relied upon for every NASA mission with an entry phase [9]. NASA Ames Research Center's arc-jet complex is the epicenter of NASA's arc-jet campaigns for entry systems testing. At Ames, the Thermophysics Facilities Branch (TSF) operates six high-power (10–60 MW) arc-heaters in four different arc-jet test bays, providing customers with high-enthalpy flows (order of MJ kg^{-1}) for extended periods of time (tens of minutes) and for various types of gas mixtures [10]. These high-powered arc jets are integral to entry missions, therefore a smaller scale arc jet facility was implemented to support development of instrumentation and diagnostics that could eventually be implemented at the high-powered facilities. This demand led to the introduction of the X-Jet in 2006, a 30 kW plasma torch setup with subsonic flow capabilities [11–14]. At the start of the ensuing decade, the X-Jet was replaced by the first generation miniature Arc-jet Research Chamber (mARC I), a 30 kW heat-sink constricted arc-heater with supersonic flow capabilities [15–17]. By 2019, mARC I evolved into mARC II through various upgrades, including, but not limited to, a larger test box, active water cooling, a new vacuum pump, and an updated data acquisition system [18].

The mARC II facility has faced challenges related to high test box pressures during operation. Initial experiments indicated that the vacuum system was unable to maintain underexpanded flow for the nozzle geometry used [19–21]. Underexpanded flow is desirable for material testing because it provides a large region of constant flow conditions. High test box pressures hinder nozzle flow expansion, which restricts testing at lower heat fluxes and limits sample

sizes. Consequently, an upgrade of the vacuum system was deemed necessary. This paper presents the results from the Integrated Systems Testing campaign conducted after installing the new vacuum system.

In §II, we provide an overview of the methods employed, including a brief description of the facility and its upgrades, the instrumentation used, key arc-jet performance metrics, and relevant numerical simulations. The results obtained are presented and discussed in §III. First, we assess the performance of the new vacuum system. Second, we present results for bulk flow enthalpy, arc-jet efficiency, and stagnation point heat flux, comparing them with measurements taken before the facility upgrades. Third, we present numerical simulation results and compare them to the experimental measurements.

This paper serves as a stepping stone for an upcoming experimental campaign where the full operational envelope of the upgraded mARC II facility will be characterized, complete with additional flow measurements and diagnostics.

II. Methods

In this section, we introduce the arc-heater and describe the facility upgrades and instrumentation used. We also review the formulations used to estimate flow enthalpy and arc-jet efficiency, and describe the method used to numerically model the experiments.

A. Arc-heater setup

The second-generation miniature Arc-jet Research Chamber (mARC II) is a 30 kW segmented constricted arc-heater developed at NASA Ames Research Center [18, 19, 21]. The mARC II facility employs a Hypertherm MAX200 plasma cutter to provide power and to control air gas flow. The system's cathode is inside the Hypertherm torch body and fully integrated within the arc-heater. For the work presented in this paper, the standard heater configuration was used with two constrictor disks (one of which has a pressure tap), an anode, and a convergent-divergent nozzle ($\varnothing 5.56$ mm throat and $\varnothing 18.67$ mm exit). There are two active water-cooling circuits: one cools the cathode torch, and the other cools the arc column, test box walls, and nozzle, as well as the newly installed diffuser and heat exchanger.

B. Facility upgrades

The mARC II facility has undergone various upgrades since the last published work [21]. These are described in this section.

1. Vacuum system

Owing to the issues with the initial vacuum system described in §I, the vacuum system was upgraded to generate and maintain an underexpanded jet for the given nozzle exit diameter.

1.1. Mechanical booster pump

A refurbished mechanical booster pump (Edwards EH4200) was procured and coupled to the existing two-stage direct drive rotary vane pump (Edwards E2M275), as shown in Fig. 1. The off-the-shelf roots blower booster pump is used to pressurize the charge going into the rotary vane vacuum pump. Both pumps are water-cooled. The diameter of the suction line from the test box to the EH4200 was increased to provide the necessary conductance for the higher pumping rates. An inlet mesh screen (ISO250, A60041571) is used to protect the EH4200 from intake debris. The outlet of the E2M275 is connected to the in-house exhaust system. The vacuum pump was designed to operate in conjunction with a new water-cooled diffuser and heat exchanger assembly to maximize the amount of heat removed with minimal pressure drop.

1.2. Diffuser & heat exchanger assembly

In tandem with the upgrade of the vacuum pump, a diffuser and a heat exchanger (HX) were designed in-house. The diffuser and heat exchanger are both water-cooled. The intent of the diffuser is to capture re-directed flow from large test samples or instrumentation devices (see Fig. 1). The heat exchanger is designed to significantly reduce the temperature of the hot gases prior to the vacuum pumps in order to prevent damage to their parts. In addition, it also reduces the volumetric flow rate (by increasing the gas density) to allow for lower vacuum pressure inside the test box. This makes the flow discharged from the arc-heater nozzle more underexpanded. This is advantageous for testing as the more underexpanded the nozzle flow is, the larger the primary test rhombus is. Lastly, the lower the test box pressure, the less re-circulating hot gases are in the test box – which can damage wiring and, to some extent, undesirably pre-heat the models.

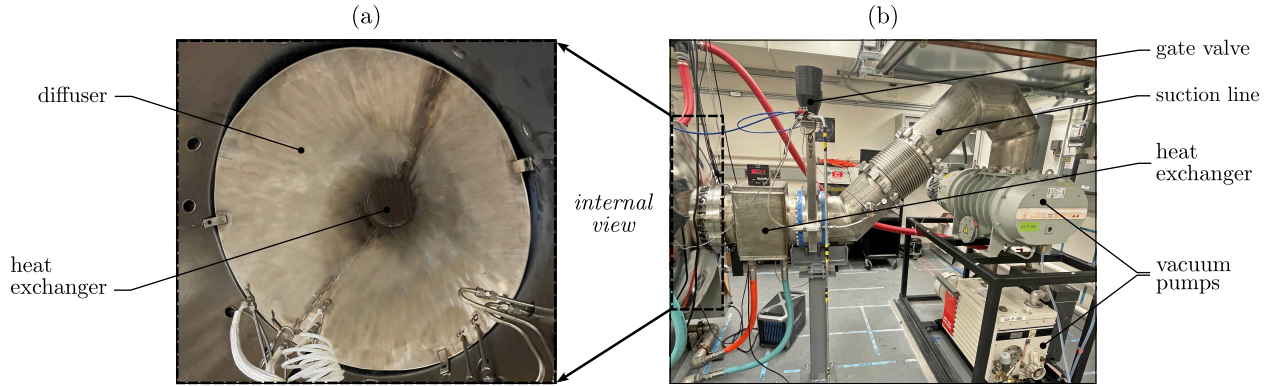


Fig. 1 Vacuum system upgrades: (a) view of the diffuser and the heat exchanger from inside the mARC II test box; (b) overview of the upgraded vacuum system, including the mechanical booster pump (Edwards EH4200) coupled to the two-stage direct drive rotary vane pump (Edwards E2M275).

2. Data acquisition system

Data bandwidth and transfer speeds have been increased from tens of MB/s to GB/s via the upgrade of several data link hardware components. The previous Ethernet port switch (Planet FSD-801) with 10–100 MB/s capability was replaced by a 1 GB/s Ethernet switch (Netgear GS308). Also, the previous USB 2.0 extender (Icron USB Ranger 2204) which used Ethernet was replaced by a USB 3.0 extender with multi-mode fiber coupling with data rates of up to 5 GB/s (Black Box IC502A-R2). These upgrades allow for higher data acquisition sampling rates, faster communication with diagnostics such as the high-speed cameras, and best-in-class electrical isolation of the data acquisition systems.

Custom printed circuit boards were developed to provide a flexible interface for a variety of facility sensors. Each board has screw terminal interfaces for 8 single-ended channels or 4 differential channels and can be vertically stacked if more channels are required. Each channel can be configured to accept single-ended voltages, differential voltages, 4–20 mA current input (via a toggleable 250 Ω resistor), and is mechanically compatible with LabJack instrumentation amplifier add-on chips. The boards also provide terminals with regulated 5 V and 24 V power for each channel. Consequently, the boards provide a convenient interface for a simple NI 9205 voltage digitizer module to read voltage, current, and low-signal inputs (thermocouple and strain gauges via instrumentation amplifier add-ons).

An in-house database application is used for data storage, visualization, and processing (Big-data Efficient and Automated Science Transfer, BEAST) [22]. Additional features for spectrum visualization, procedure version control/tracking, and additional statistical tracking have been added in the past year.

C. Instrumentation

Measurements of arc-jet facility data, such as arc current, arc voltage, supply gas mass flow rate, arc column pressure, and test box pressure are acquired during all experiments at a sampling rate of 12.5 Hz. A sweep arm is used to house the flow measurement sensors [21]. The sweep arm is wrapped using Refrasil silica material to protect the sweep arm from the high-temperature nozzle flow. A constant sweep arm rotational speed of 50 rpm is used for all the runs presented in this work (for a sweep arm length of 127 mm). Stagnation point heat flux measurements are made using a water-cooled Gardon gauge with a $\varnothing 4.76$ mm (3/16") hemispherical copper body (Medtherm, 12-3000-1.0-6-72-21631T) at 70 mm from the nozzle exit plane (maximum possible distance with the current setup). This stagnation point heat flux probe is dwelled for 1 s for each condition and is the mARC II reference stagnation point heat flux sensor. A high-pressure water cooling system is employed to keep the Gardon gauge within acceptable temperatures [21]. A range of different sampling rates f_s (80 Hz, 500 Hz, and 8000 Hz) is used for the collection of calorimeter data in this work to assess how f_s affects the quality of the heat flux signal (see §III.C).

Table 1 lists all the instruments used to make measurements in this work.

D. Arc-jet performance

Critical parameters in arc-jet performance characterization include bulk enthalpy and arc-jet efficiency. In this section, we present these metrics and how they are computed using data obtained from experimental measurements.

Table 1 List of measurements presented in this work and relevant instrumentation used during mARC II operation.

Measurement	Symbol	Instrumentation
Arc column static pressure	p_{col} [kPa]	Setra Model 730 capacitance manometer
Arc current	I_{arc} [A]	Ohio Semitronics CTL-401S/300 current transducer Ohio Semitronics CTA 201H signal conditioner
Arc voltage	V_{arc} [V]	Ohio Semitronics VT7-007E-11-TP voltage transducer
Post-heat exchanger static pressure	p_{HX} [Pa]	KJLC 345 Series Pirani Gauge
Post-heat exchanger temperature	T_{HX} [K]	Omega TJC360-CPSS-062U-8 thermocouple
Stagnation point heat flux	\dot{q} [W cm ⁻²]	Medtherm water-cooled Gardon gauge (\varnothing 4.76 mm hemispherical)
Supply gas (air) mass flow rate	\dot{m} [g s ⁻¹]	Sage SIP-030-DC24-AIR thermal flow meter
Test box static pressure	p_{∞} [Pa]	Inficon SKY CDG025D capacitance manometer (1000 torr) Inficon SKY CDG025D capacitance manometer (10 torr)
Water flow rate	\dot{m}_w [g s ⁻¹]	Omega G2S20NQ9GMB turbine flow meter
Water temperature change	ΔT_w [K]	E & C Co., Thermoducer 8 (17 Ω , 3000 psi)

1. Bulk flow enthalpy

1.1. Enthalpy by energy balance (EB²)

Bulk enthalpy is estimated from the arc power P_{arc} and the power lost in the arc-heater cooling circuits ΔP_{cool} :

$$\bar{h}_{\text{EB}^2} = \frac{P_{\text{arc}} - \Delta P_{\text{cool}}}{\dot{m}} = \frac{P_{\text{arc}} - \Delta P_{\text{cathode}} - (\Delta P_{\text{anode}} + \Delta P_{\text{disks}} + \Delta P_{\text{nozzle}})}{\dot{m}}, \quad (1)$$

where:

$$P_{\text{arc}} = I_{\text{arc}} V_{\text{arc}}, \quad \Delta P_{\text{cathode}} \simeq 0, \quad \Delta P_{\text{anode}} + \Delta P_{\text{disks}} + \Delta P_{\text{nozzle}} = \dot{m}_w c_{p,w} \Delta T_w, \quad (2a-c)$$

where I_{arc} is the arc current, V_{arc} is the arc voltage, \dot{m} is the mass flow rate of air, \dot{m}_w is the cooling water mass flow rate, ΔT_w is the temperature difference between the water supply and return lines, and $c_{p,w} = 4179 \text{ J kg}^{-1} \text{ K}^{-1}$ is the isobaric specific heat capacity of water [23, 24].

In the EB² (or EB2) bulk enthalpy estimation technique, the \dot{m}_w and ΔT_w are the two variables driving the enthalpy estimation. Equation (1) accounts for losses across the full arc-heater since the column constrictor disk walls, anode, and nozzle are actively cooled. We assume the power losses at the cathode $\Delta P_{\text{cathode}}$ to be negligible due to the cathode surface area being small ($\varnothing < 1 \text{ mm}$) – this assumption will be studied in future work.

1.2. Enthalpy by sonic flow method and empirical correlations

Data from EB² measurements is necessary for deriving empirical correlations and is useful in comparing the performance of different arc-jet facilities. Thompson, Prabhu, et al. [25] derived a semi-empirical bulk enthalpy (\bar{h}^T) correlation based on equilibrium thermodynamics for various gas conditions using EB² data from NASA Ames' Aerodynamic Heating Facility (AHF) and Interaction Heating Facility (IHF):

$$\bar{h}^T = \left(\frac{155.8}{\sigma} \right)^2, \quad \sigma = \frac{\dot{m}}{A_t p_{0,\text{col}}}, \quad (3a-b)$$

where σ is the sonic flow parameter ($\text{kg m}^{-2} \text{ atm}^{-1}$), \dot{m} is the mass flow rate of air (kg s^{-1}), A_t is the nozzle throat area (m^2), and $p_{0,\text{col}}$ is the stagnation pressure in the arc column (bar). This formulation differs from the popular sonic flow methods of Winovich [26] (\bar{h}^W) and Shepard et al. [27] (\bar{h}^S), respectively:

$$\bar{h}^W = \left(\frac{123}{\sigma} \right)^{2.52}, \quad \bar{h}^S = \left(\frac{158.7}{\sigma} \right)^{1.971}. \quad (4a-b)$$

Thompson, Prabhu, et al. [25] claim the work of Winovich [26] over-predicts enthalpy for low mass flow rates and that their formulations offers the same levels of accuracy as Winovich [26] and Shepard et al. [27] over a larger dataset (1000+ cases). The correlation constants have been demonstrated to be facility dependent, which could be evidence for a dependence on arc column diameter, nozzle exit diameter, and/or other geometrical dimensions and/or flow properties not accounted for in the sonic flow parameter σ .

2. Arc-jet efficiency

A measure of effective arc-jet efficiency can be formulated based on the conversion of specific input energy into bulk enthalpy:

$$\eta = \frac{\bar{h}}{P_{\text{arc}}/\dot{m}}. \quad (5)$$

E. Numerical simulations

Fully laminar Navier–Stokes simulations were performed using the Data Parallel Line Relaxation (DPLR) code, v4.04 [28]. DPLR is a NASA solver developed by the Entry Systems and Technology Division at NASA Ames Research Center to simulate supersonic and hypersonic aerothermal flows in chemical and thermal non-equilibrium.

An axisymmetric computational domain is employed comprising of the last section of the arc column, the nozzle, part of the test box, and the Gardon gauge geometry. A fully catalytic isothermal boundary condition (350 K) was implemented for the arc-heater column, nozzle, and Gardon gauge surfaces. The NASA Chemical Equilibrium Applications (CEA) code was used to derive uniform freestream boundary conditions for the inlet and outlet of the domain [29]. Specifically, for each of the two freestreams (high-pressure inlet and low-pressure outlet), we impose velocity, density, temperature, and mass fraction conditions, whereby a 5-species air mixture (N_2 , O_2 , NO , N , O) was assumed [30, 31]. These four flow properties are obtained as outputs from CEA using either enthalpy and pressure or temperature and pressure as initial conditions.

For the high-pressure inlet, Eq. (4)a is used to calculate the flow enthalpy from the experimentally-measured arc column pressure \bar{p}_{col} and mass flow rate \dot{m} . The calculated flow enthalpy \bar{h} and measured arc column pressure \bar{p}_{col} are then used as inputs to CEA. For the low-pressure outlet, we assume a static temperature of 300 K and use the experimentally-measured test box pressure \bar{p}_{∞} as inputs to CEA.

III. Results

A. Performance of the new vacuum system

With the previous vacuum system, the mARC II test box reached a 53 Pa base pressure after 35 mins of pumping. With the upgraded vacuum system, the mARC II test box is now able to reach a steady-state base pressure of 4 Pa after 15 mins of pumping. This equates to a 2X improvement in pump-down time to base pressure and a 13X improvement in base pressure prior to gas addition. Under test conditions, the upgraded vacuum system is now able to generate and successfully maintain underexpanded flow conditions. Recall that with the previous vacuum system, the addition of gas significantly increased the test box pressure, resulting in an overexpanded jet that was undesirable for testing [20, 21].

Extensive numerical analyses were performed throughout the design process using computational fluid dynamics (CFD). The performance of the heat exchanger was verified experimentally, showing positive agreement with the design calculations, as shown in Table 2.

Table 2 Comparison between experimental measurements and CFD design models for the performance of the upgraded vacuum system.

Measurement	Experimental	Design CFD	$ \delta $
Average test box static pressure \bar{p}_{∞}	60 Pa	52 Pa	13%
Average post-heat exchanger static pressure \bar{p}_{HX}	67 Pa	69 Pa	3%
Maximum post-heat exchanger temperature T_{HX}	303 K	293 K	3%

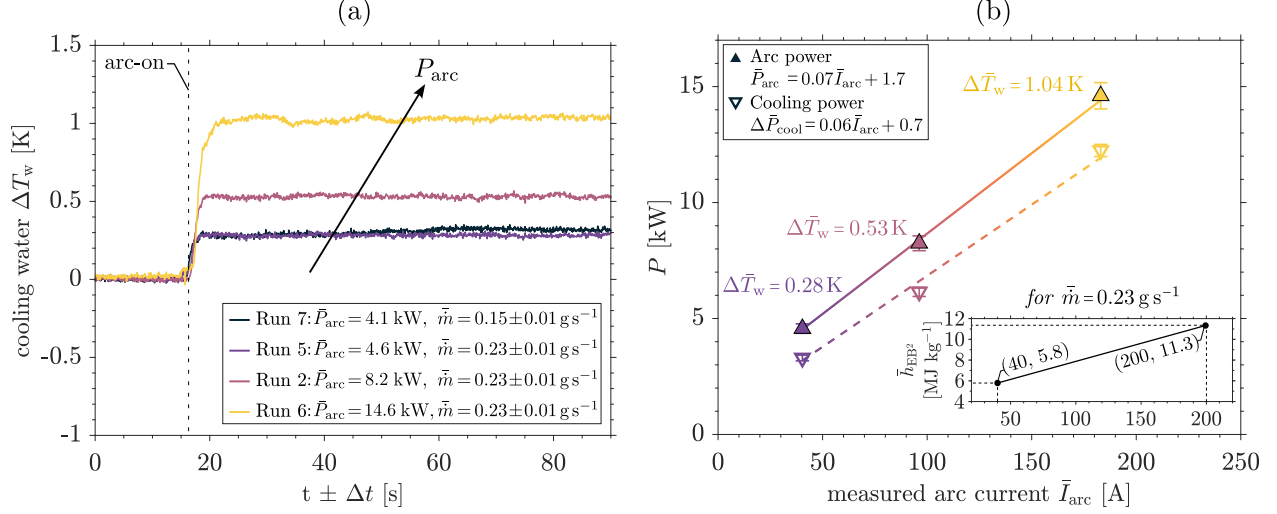


Fig. 2 Data used to compute bulk enthalpy via energy balance (EB 2) method: (a) change in cooling water temperature ΔT_w for runs 2, 5, 6, and 7; (b) arc power \bar{P}_{arc} and cooling power loss $\Delta \bar{P}_{\text{cool}}$ as a function of arc current \bar{I}_{arc} for runs 2, 5, and 6 ($\bar{m} = 0.23$ g s $^{-1}$) – inset shows the linear relationship between arc current \bar{I}_{arc} and EB 2 bulk enthalpy \bar{h}_{EB^2} .

B. Bulk flow enthalpy

In this section, we report EB 2 enthalpy values obtained in mARC II for the first time. As described in §II.D.1, the cooling water flow rate \dot{m}_w and the temperature difference ΔT_w between the water supply and return lines drive the calculation of the bulk enthalpy. However, the water flow rate is constant for all cases ($\dot{m}_w \approx 2.79 \pm 0.05$ kg s $^{-1}$). As such, in Fig. 2(a) we plot the the key driver of the enthalpy calculation, which is the cooling water temperature change ΔT_w . The time vector for each run has been adjusted by $\pm \Delta t$ in order to align the arc-on times for all runs. The temperature change for each run is averaged over 20 s during steady-state to obtain the average temperature change $\Delta \bar{T}_w$ – values for three conditions are shown in Fig. 2(b).

Figure 2(b) shows arc power \bar{P}_{arc} and power lost to cooling $\Delta \bar{P}_{\text{cool}}$ as a function of measured arc current \bar{I}_{arc} for $\bar{m} = 0.23$ g s $^{-1}$. Both variables demonstrate a linear relationship with \bar{I}_{arc} , as shown in the figure legend. A weighted

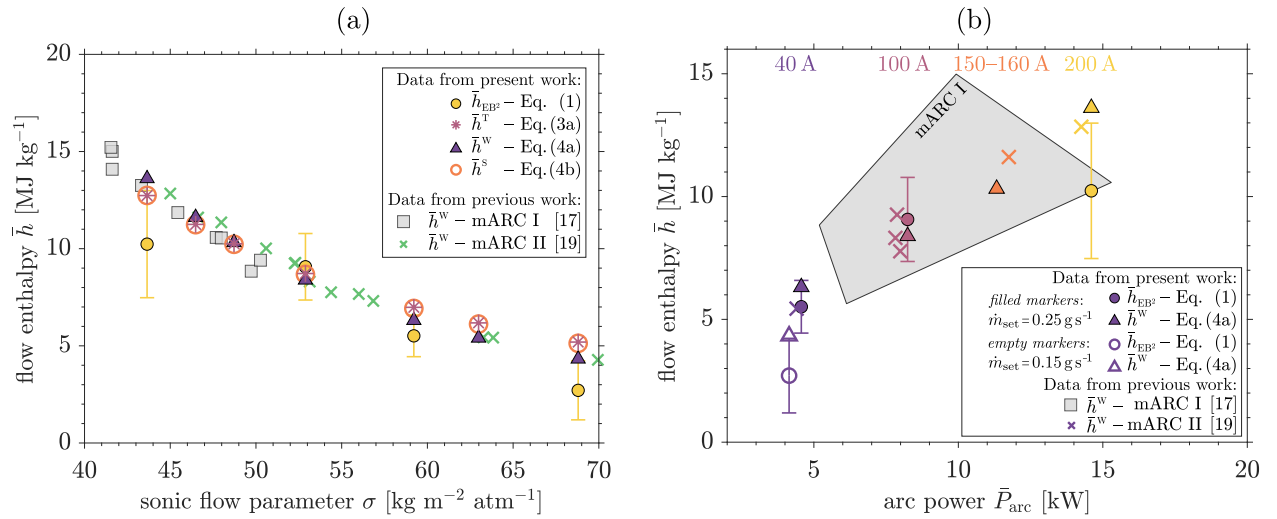


Fig. 3 Flow enthalpy \bar{h} generated by mARC II with the new vacuum system compared to mARC I (for all \dot{m}_{set}) [17] and mARC II with the previous vacuum system (for $\dot{m}_{\text{set}} = 0.25$ g s $^{-1}$) [19]: (a) as a function of sonic flow parameter σ ; (b) as a function of arc power \bar{P}_{arc} .

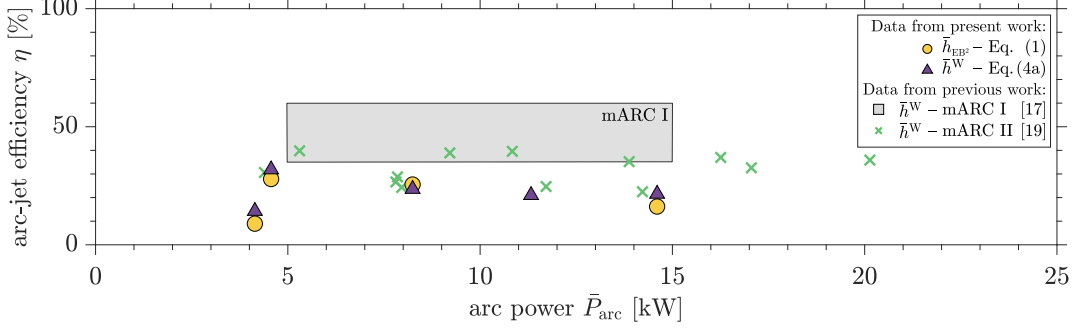


Fig. 4 Arc-jet efficiency η as a function of arc power \bar{P}_{arc} : mARC II with new vacuum system compared to mARC I [17] and mARC II with the previous vacuum system [19].

least-squares fit using $1/\sigma_x^2$ as the weight was employed for the fits (where x is \bar{P}_{arc} or $\Delta\bar{P}_{\text{cool}}$). The data used in the fits was limited to runs with voltage readings. Run 3 is considered an outlier and not shown. It should be noted that the difference between the set arc current I_{set} and measured arc current \bar{I}_{arc} has been discussed in previous work [19, 21].

Based on the initial dataset for mARC II presented in Fig. 2(b), we propose that – for a constant working gas mass flow rate \dot{m} – the EB² bulk flow enthalpy \bar{h}_{EB^2} follows a linear relationship with measured arc current \bar{I}_{arc} (assuming negligible cathode power losses). For a measured air mass flow rate of $\bar{m} = 0.23 \text{ g s}^{-1}$, we can input the linear fits presented in Fig. 2(b) into Eq. (1) to get:

$$\bar{h}_{\text{EB}^2}^{0.23 \text{ g s}^{-1}} \simeq \frac{(69.3\bar{I}_{\text{arc}} + 1733) - (61.3\bar{I}_{\text{arc}} + 714.3)}{0.23 \times 10^{-3}} = \frac{7.99\bar{I}_{\text{arc}} + 1018.7}{0.23 \times 10^{-3}}. \quad (6)$$

where the units for power have been changed from kilowatt to watt. Using Eq. (6), we estimate that mARC II generates bulk enthalpies \bar{h}_{EB^2} between 5.8 MJ kg^{-1} and 11.3 MJ kg^{-1} for a measured air mass flow rate of $\bar{m} = 0.23 \text{ g s}^{-1}$, as shown in the inset of Fig. 2(b).

In Fig. 3(a), we plot the flow enthalpy \bar{h} as a function of sonic flow parameter σ , as defined by Eq. (3)b. Enthalpy computed with sonic flow method correlations for the present work shows good agreement with data for mARC I and mARC II with the previous vacuum system [17, 19]. Three of the four EB² enthalpy data points are lower than those calculated using correlations. This could be due to losses in the EB² setup or it could be an indication that the correlations do not fully capture the behavior in smaller-scale arc-jet facilities, such as mARC II. This will be investigated in future work. Error bars represent the standard deviation in the EB² measurements, with their magnitude currently constrained by the facility data sampling rate ($f_s = 12.5 \text{ Hz}$). Improvements to this limitation are underway. Fig. 3(b) compares flow enthalpy \bar{h} as a function of arc power \bar{P}_{arc} . Due to the active cooling of the arc-heater, mARC II can attain lower enthalpies compared to mARC I. The addition of a third constrictor disk would enable mARC II to reach even higher enthalpies. This will also be investigated in future work.

Lastly, Fig. 4 shows the efficiency η of mARC II with the new vacuum system, comparing its performance with that of previously published data for mARC I and mARC II with the previous vacuum system. The results are in agreement with the previous mARC II iteration. Inspecting the arc-jet efficiency η values computed using the Winovich [26] bulk enthalpy \bar{h}^w , we report efficiencies between 14% and 32% for the data collected in the present work. Initial data suggests that a combination of low current and high flow rate leads to the highest mARC II efficiency.

The comparisons presented are preliminary due to the limited data points available. A more thorough discussion will be detailed upon completion of the characterization campaign of the full operational envelope.

C. Stagnation point heat flux

Figure 5(a) shows the time-resolved heat flux signal for run 5 ($\bar{I}_{\text{arc}} = 40 \text{ A}$, $\bar{m} = 0.23 \text{ g s}^{-1}$) sampled at $f_s = 8000 \text{ Hz}$. Figure 5(b) illustrates the high frequency content of the calorimeter signal. We identify four major peaks in the frequency spectra at 300 Hz, 600 Hz, 800 Hz, and 1600 Hz, with the 600 Hz and 1600 Hz peaks likely being second harmonics of the others. Higher frequencies have been filtered out using a low-pass Butterworth filter with a 40 Hz cut-off frequency (the rise time of the raw signal was captured), as AC signals are not of interest to our analysis and are associated with interference from other sources in mARC II.

In this work, we utilized three different sampling frequencies f_s for the Gardon gauge data collection (80 Hz, 500 Hz, and 8000 Hz) to assess how this would affect the signal-to-noise ratio (SNR) (see Table 3 in the appendix). As shown in

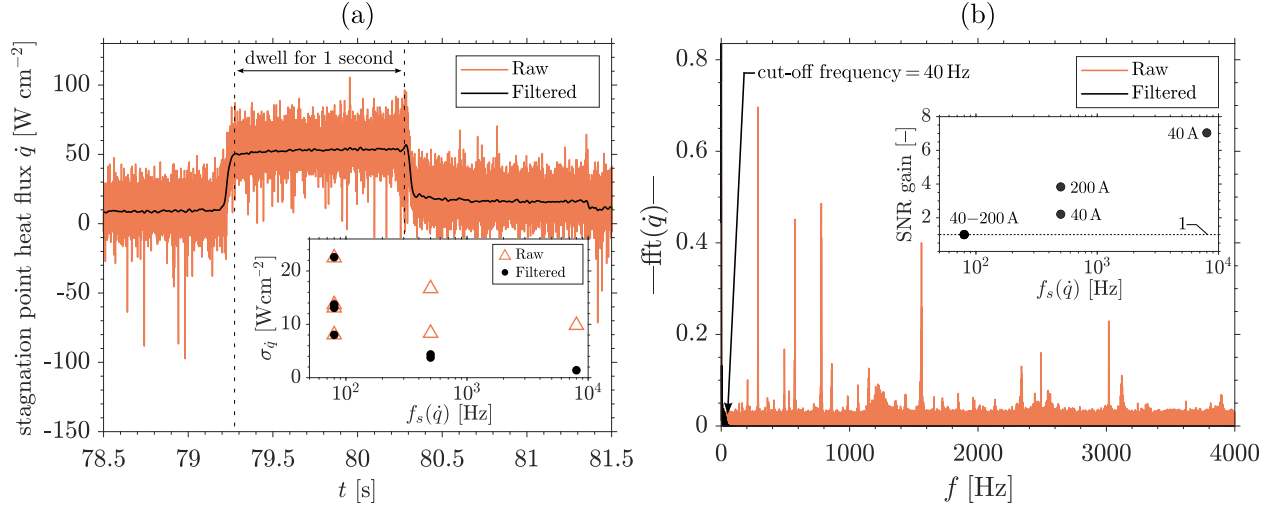


Fig. 5 Stagnation point heat flux \dot{q} measurements using a water-cooled Gardon gauge ($\varnothing 4.76$ mm, 3/16" hemispherical) for run 5 ($\bar{I}_{\text{arc}} = 40$ A, $\bar{m} = 0.23$ g s $^{-1}$): (a) time series with and without low-pass Butterworth filter ($f_c = 40$ Hz) – inset shows standard deviation of heat flux signal $\sigma_{\dot{q}}$ during steady-state dwell as a function of sampling frequency $f_s(\dot{q})$ with and without low-pass filtering (data from all runs included in inset); (b) single-side amplitude of fast-Fourier transform with and without low-pass filtering ($f_c = 40$ Hz) – inset shows gain in signal-to-noise ratio (SNR) of the average heat flux \bar{q} by using low-pass filtering as a function of sampling frequency $f_s(\dot{q})$ (data from all runs included in inset).

the inset for Fig. 5(a), a low-pass filter will only reduce the standard deviation of the heat flux signal $\sigma_{\dot{q}}$ if the sampling rate f_s is high enough. At $f_s = 500$ Hz, a gain in SNR is clear when using the low-pass filter (see inset for Fig. 5(b)). To improve the SNR of the raw signal, the sampling rate has to be high. For future characterization campaigns, we will use the highest sampling rate possible (8000 Hz is currently the maximum) along with the low-pass filter in post-processing to maximize the SNR of the heat flux measurements.

Figure 6(a) shows the average stagnation point heat flux \bar{q} measured as a function of bulk flow enthalpy \bar{h} . The average stagnation point heat flux \bar{q} is obtained by averaging the stagnation point heat flux \dot{q} over the steady-state dwell time. The performance of mARC II with the upgraded vacuum system is contrasted with that of both mARC I and

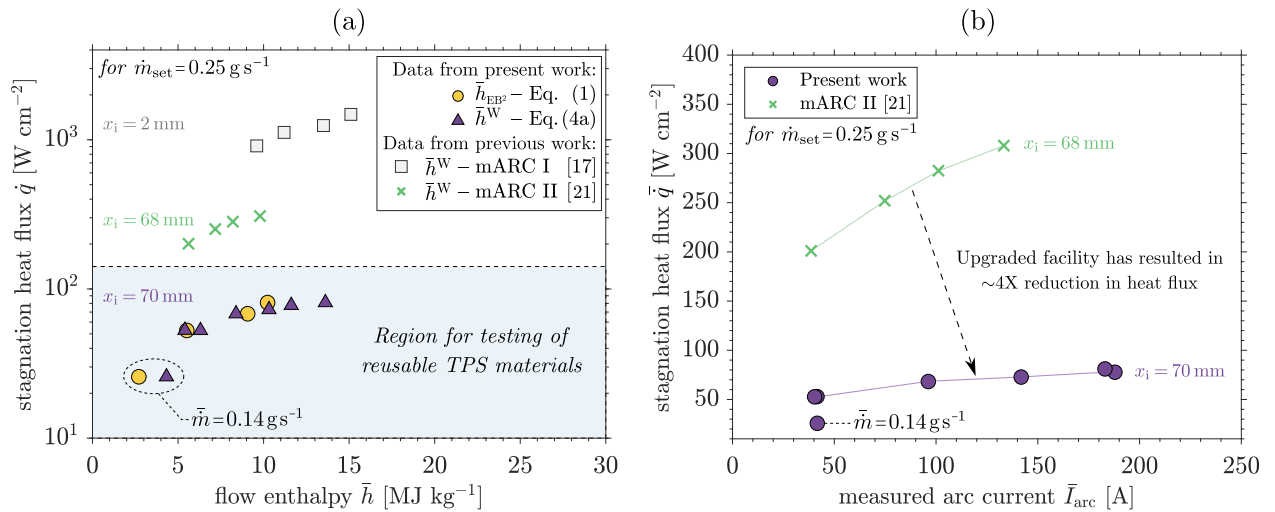


Fig. 6 Stagnation point heat flux \bar{q} measurements using a water-cooled Gardon gauge ($\varnothing 4.76$ mm, 3/16" hemispherical) for $\dot{m}_{\text{set}} = 0.25$ g s $^{-1}$ as a function of: (a) flow enthalpy \bar{h} ; (b) arc current \bar{I}_{arc} .

mARC II with the previous vacuum system, examining cases where the flow rate is $\dot{m}_{\text{set}} = 0.25 \text{ g s}^{-1}$ and the calorimeter distance from the nozzle exit plane is 2 mm, 68 mm, or 70 mm, depending on the facility. As shown in Fig. 6(a), we report for the first time heat fluxes below 200 W cm^{-2} . Specifically, 25.8 to 81.0 W cm^{-2} for sonic flow enthalpies ranging between 4.3 and 13.6 MJ kg^{-1} . The minimum heat flux was measured in run 7 at the lowest current and mass flow rate condition studied ($\bar{I}_{\text{arc}} = 42 \text{ A}$, $\bar{m} = 0.14 \text{ g s}^{-1}$). It should be acknowledged that the current iteration of mARC II is expected to feasibly generate heat fluxes comparable to those published for mARC I at 2 mm from the nozzle exit (kW cm^{-2}). This is anticipated under test conditions where the set current and flow rates are maximized, and the trident distance from the nozzle exit plane is minimized. Such test conditions will be included in the upcoming characterization campaign. The results presented demonstrate that mARC II could be employed for the testing of thermal protection systems (TPS) that require low heating rates (e.g., reusable TPS materials).

Figure 6(b) shows the average stagnation point heat flux \bar{q} measured as a function of measured arc current \bar{I}_{arc} . The performance of mARC II with the upgraded vacuum system is contrasted with that of mARC II with the previous vacuum system, examining cases where the set flow rate is $\dot{m}_{\text{set}} = 0.25 \text{ g s}^{-1}$ and the calorimeter distance from the nozzle exit plane is similar for both facilities (68 mm or 70 mm). This comparison highlights the direct impact that the vacuum system upgrade had on the operational envelope of the facility. There is an approximate 4X reduction in measured stagnation point heat flux \bar{q} for the same set test conditions [21]. This is attributed to the underexpanded flow generated by the new vacuum system.

D. Laminar Navier–Stokes numerical simulations

Figure 7 shows the numerical solutions for flow enthalpy \bar{h} and Mach number M for run 1 ($\bar{I}_{\text{arc}} = 42 \text{ A}$, $\bar{m} = 0.23 \text{ g s}^{-1}$). In Fig. 7(a), the radial enthalpy gradient is steep and clear owing to heat conduction to the walls. Nawaz et al. [17] also identified this via numerical simulations of mARC I. Since mARC I was not water-cooled, the radial enthalpy gradient is assumed to be amplified in mARC II. As seen in experiments, the simulations predict an underexpanded nozzle flow, as needed to match the test box pressure. In Fig. 7(b), the formation of a Mach disk is not identifiable. As such, it is presumed to be formed downstream of the Gardon gauge (and the computational domain) for the conditions tested.

Stagnation point heat flux \bar{q} predictions at the Gardon gauge location were extracted from the numerical simulations for comparison with experimental measurements. A summary of the numerical solutions for heat flux \bar{q} are shown in Table 3. The modeled stagnation point heat flux \bar{q} agrees within 3% for run 1 ($\bar{I}_{\text{arc}} = 42 \text{ A}$, $\bar{m} = 0.23 \text{ g s}^{-1}$) and 15% for run 7 ($\bar{I}_{\text{arc}} = 42 \text{ A}$, $\bar{m} = 0.14 \text{ g s}^{-1}$). However, the discrepancy between measured and predicted values increases with arc power \bar{P}_{arc} to a maximum difference of 49% for run 4 ($\bar{I}_{\text{arc}} = 188 \text{ A}$, $\dot{m}_{\text{set}} = 0.23 \text{ g s}^{-1}$ condition). Further work will be undertaken to understand the reasons behind this trend.

A summary of the results from the present work can be found in Table 3 in the appendix.

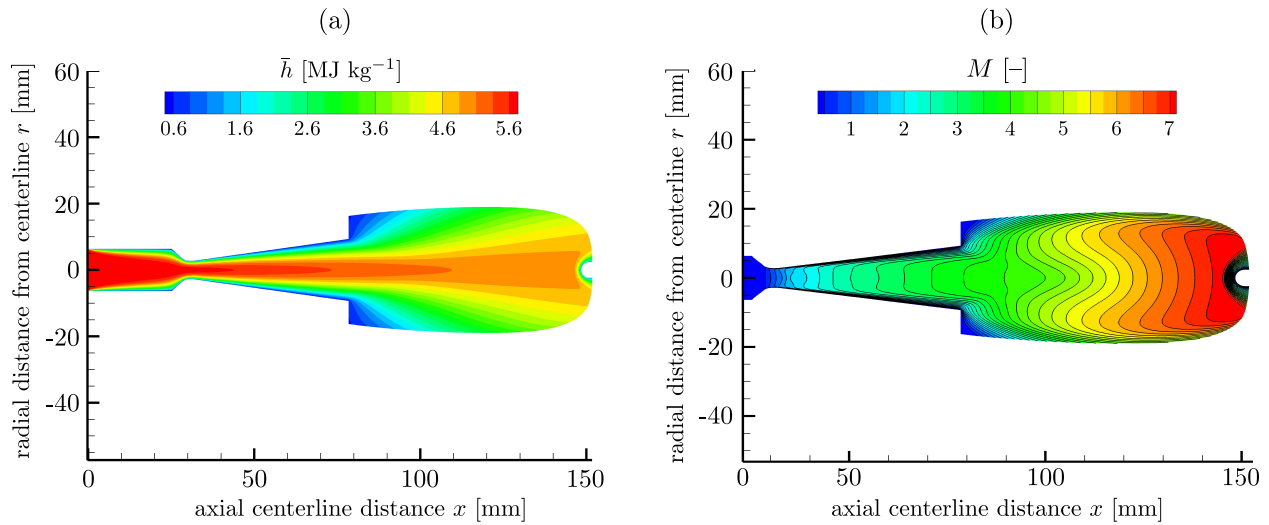


Fig. 7 Laminar axisymmetric Navier–Stokes solutions for run 1 ($\bar{I}_{\text{arc}} = 42 \text{ A}$, $\bar{m} = 0.23 \text{ g s}^{-1}$): (a) flow enthalpy \bar{h} ; (b) Mach number M .

IV. Conclusion

An Integrated Systems Testing campaign was undertaken for the 30 kW mARC II arc-jet facility at NASA Ames Research Center after the completion of facility upgrades. These upgrades were necessary because the previous vacuum system could not maintain constant test box pressure for the current nozzle, leading to undesirable overexpanded flow. This issue has been resolved by installing a new vacuum system, including a diffuser, heat exchanger, and mechanical booster vacuum pump. The upgrades to the vacuum system significantly improved mARC II's performance, enabling it to sustain underexpanded flow during tests and generate lower heat fluxes. The heat flux, measured by a water-cooled Gardon gauge ($\varnothing 4.76$ mm, 3/16" hemispherical) at 70 mm from the nozzle exit plane, was reduced by $\sim 4X$ under test conditions matching those of prior experiments with the previous vacuum system. Notably, we report the lowest stagnation point heat fluxes measured in mARC II to date, ranging from 25.8 to 81.0 W cm⁻². This work provides an initial demonstration that mARC II could facilitate the development of novel TPS technologies (e.g., reusable TPS) by confirming its capability for low heat flux testing. In conjunction with experimental measurements, the NASA DPLR Navier–Stokes code was used to obtain numerical stagnation point heat flux results. The laminar axisymmetric simulations agreed well at the lowest arc power conditions, but discrepancy increased with arc power (3–15% at $\bar{I}_{\text{arc}} = 42$ A to 49% at $\bar{I}_{\text{arc}} = 188$ A). Future work will involve full characterization of the operational envelope of mARC II and include measurements using a coaxial calorimeter for radial heat flux profiles and a Pitot probe for stagnation pressure. These experimental measurements will be used to support validation of additional numerical modeling efforts.

Estimates for bulk enthalpy using an energy balance method (EB²) were presented for the first time using data collected in mARC II. The preliminary data presented in this work indicates that using EB² results in lower bulk enthalpy values ($2.7 \leq \bar{h} \leq 10.2$ MJ kg⁻¹) than those using sonic flow theory or empirical correlations derived for larger-scale arc-jet facilities ($4.3 \leq \bar{h} \leq 13.6$ MJ kg⁻¹ using the Winovich equation). Data from future mARC II experimental campaigns will be used to assess the validity of existing correlations more concretely and to derive an empirical correlation specific to mARC II.

Appendix

A summary of the test cases and select experimental outputs obtained for this work is shown in Table 3.

Table 3 Test matrix and outputs for standard mARC II configuration S (two constrictor disks). In order of left to right for each case, we have data relevant to the arc column, the instrumentation, and the numerical simulations using the NASA DPLR code. For the arc column, we include the set air mass flow rate \dot{m} , the set arc current I_{set} , a mark to indicate if a stable arc-on was generated after three attempts, the average steady-state air mass flow rate \bar{m} , the average steady-state arc current \bar{I}_{arc} , the average steady-state arc power \bar{P}_{arc} , and the average steady-state arc column pressure \bar{p}_{col} . For the operational envelope results, we include the average steady-state text box pressure \bar{p}_{∞} , the distance of the Gardon gauge from the nozzle exit plane x_i , the average steady-state heat flux measured by the Gardon calorimeter \bar{q} , the signal-to-noise ratio of the heat flux measurement $\text{SNR}(\bar{q})$, the sampling frequency of the heat flux measurement $f_s(\dot{q})$, the sonic flow enthalpy \bar{h}^W calculated using the Winovich equation [26], the mean flow enthalpy estimated via energy balance \bar{h}_{EB^2} , and the arc-jet efficiency η (using the bulk enthalpy \bar{h}^W equation by Winovich [26]). For the DPLR simulations, we include the predicted stagnation point heat flux \bar{q} and the absolute difference relative to the experimentally measured value $|\delta\bar{q}|$.

Run	Arc column							Operational envelope (two constrictor disks)							DPLR CFD		
	\dot{m}_{set} [g s ⁻¹]	I_{set} [A]	Arc-on [-]	\bar{m} [g s ⁻¹]	\bar{I}_{arc} [A]	\bar{P}_{arc} [kW]	\bar{p}_{col} [kPa]	\bar{p}_{∞} [Pa]	x_i [mm]	\bar{q} [W cm ⁻²]	$\text{SNR}(\bar{q})$ [-]	$f_s(\dot{q})$ [Hz]	\bar{h}^W [MJ kg ⁻¹]	\bar{h}_{EB^2} [MJ kg ⁻¹]	η [%]	\bar{q} [W cm ⁻²]	$ \delta\bar{q} $ [%]
1	0.25	40	✓	0.23	42	–	15	16	70	53	6.6	80	5.4	–	–	55	3%
2	0.25	100	✓	0.23	96	8.2	18	17	70	68	5.2	80	8.4	9.1	24	85	25%
3	0.25	150	✓	0.23	142	11	20	18	70	73	5.3	80	10.3	–	21	104	43%
4	0.25	200	✓	0.23	188	–	21	18	70	78	3.4	80	11.6	–	–	116	49%
5	0.25	40	✓	0.23	40	4.6	16	17	70	53	38	8000	6.3	5.5	32	–	–
6	0.25	200	✓	0.23	183	15	22	19	70	81	19	500	13.6	10	22	–	–
7	0.15	40	✓	0.14	42	4.1	8.3	13	70	26	6.8	500	4.3	2.7	14	22	15%

Acknowledgments

J. Rodrigues is the recipient of a NASA Postdoctoral Program (NPP) research fellowship at NASA Ames Research Center, administered by Oak Ridge Associated Universities (ORAU) under contract with NASA. S. Colom is supported through the NASA NNA15BB15C contract. R. Chung and J. Hartman are supported through the NASA 80ARC022DA011 contract. The authors would like to thank James Hope, Rommel Mallorca, Matthew Hoffer, Juan Tapia, Alejandro Contreras, Pedro Solano, Nicholas Reed, Jacob Weiland, Richard Ryzinga, and Casey Ching for the implementation of the facility upgrades. Lastly, thank you to Andrew Morgan (NSWCDD Reentry Systems Office) for help with the design and analysis of the vacuum system upgrade.

References

- [1] Karl, S., and Bykerk, T., “Sustainable space technologies—Strategies toward a predictive aerothermal design of re-useable space transportation systems,” *Review of Scientific Instruments*, Vol. 95, No. 2, 2024.
- [2] MacDonald, M. E., Balboni, J., Cornelison, C., Hartman, J., Haw, M., Fretter, E., Cruden, B., Wilder, M., and Hwang, H., “NASA Ames Thermophysics Ground Test Facilities Supporting Future Planetary Atmospheric Entry,” *Bulletin of the AAS*, Vol. 53, No. 4, 2021.
- [3] Lundell, J. H., Otten, L. J., and Dickey, R. R., “The CO₂ gasdynamic laser as a high-intensity radiation facility,” *13th Aerospace Sciences Meeting*, AIAA, Pasadena, California, 1975, p. 177.
- [4] Winovich, W., and Carlson, W. C. A., “The 60-MW Shuttle Interaction Heating Facility,” *Proceedings of the 25th International Instrumentation Symposium*, ISA, Pittsburgh, Pennsylvania, 1979, p. 59–75.
- [5] Balter-Peterson, A., Nichols, F., Mifsud, B., and Love, W., “Arc jet testing in NASA Ames Research Center thermophysics facilities,” *AIAA 4th International Aerospace Planes Conference*, AIAA, Orlando, Florida, 1992, p. 5041.
- [6] Wilder, M. C., Bogdanoff, D. W., and Cornelison, C. J., “Hypersonic Testing Capabilities at the NASA Ames Ballistic Ranges,” *53rd AIAA Aerospace Sciences Meeting*, AIAA, Kissimmee, Florida, 2015, p. 1339.
- [7] Cushman, G., Alunni, A., Balboni, J., Zell, P., Hartman, J., and Empey, D., “The Laser Enhanced Arc-Jet Facility (LEAF-Lite): Simulating Convective and Radiative Heating with Arc-jets and Multiple 50-kW CW Lasers,” *2018 Joint Thermophysics and Heat Transfer Conference*, AIAA, Atlanta, Georgia, 2018, p. 3273.
- [8] MacDonald, M., Rodrigues, J., Cushman, G., Martin, K., and Hartman, J., “Simultaneous Convective and Radiative Heating of Materials with the 200 kW Laser Enhanced Arc Jet Facility (LEAF),” *National Space & Missile Materials Symposium and Commercial and Government Responsive Access to Space Technology Exchange (NSMMS & CRAFT) Joint Symposia*, Tucson, Arizona, 2023, pp. 1–18.
- [9] Calomino, A., Bruce, W., Gage, P., Horn, D., Mastaler, M., Rigali, D., Robey, J., Voss, L., Wahlberg, J., and Williams, C., *Evaluation of the NASA Arc Jet Capabilities to Support Mission Requirements [NASA/SP-2010-577]*, 2010.
- [10] Terrazas-Salinas, I., *Test Planning Guide for NASA Ames Research Center Arc Jet Complex and Range Complex [A029-9701-XM3 Rev. J – July 28, 2022]*, 2022.
- [11] Fu, J., Olivares, R., Oishi, T., Martinez, E., and Gorbunov, S., “XJet: A Small-Scale Aerothermal Test Environment for Instrumentation,” *44th AIAA Aerospace Sciences Meeting and Exhibit*, AIAA, Reno, Nevada, 2006, p. 1321.
- [12] Beck, R. A., White, S., Arnold, J., Fan, W., Stackpoole, M., Agrawal, P., and Coughlin, S., “Overview of Initial Development of Flexible Ablators for Hypersonic Inflatable Aerodynamic Decelerators,” *21st AIAA Aerodynamic Decelerator Systems Technology Conference and Seminar*, AIAA, Dublin, Ireland, 2011, p. 2511.
- [13] Fan, W., Thornton, J., Chavez-Garcia, J., Beck, R., and Ghandehari, E., “Charring Behavior of Lightweight Silicone-based Ablators,” *43rd AIAA Thermophysics Conference*, AIAA, New Orleans, Louisiana, 2012, p. 2746.
- [14] White, S., “Effects of Laser Wavelength on Ablator Testing,” *38th Annual Conference on Composites, Materials and Structures*, Cape Canaveral, Florida, 2014.
- [15] Codron, D. A., and Nawaz, A., “Radial Profiles of Plasma Electron Characteristics in a 30 kW Arc Jet,” *44th AIAA Plasmadynamics and Lasers Conference*, AIAA, San Diego, California, 2013, p. 3128.
- [16] Codron, D. A., Cruden, B. A., and Ho, T., “Emission Spectroscopy Characterization of Thermal Protection System Materials in Arc-Heated Flows,” *45th AIAA Plasmadynamics and Lasers Conference*, AIAA, Atlanta, Georgia, 2014, p. 2112.

- [17] Nawaz, A., Ho, T. S., Philippidis, D., MacDonald, M., McGlaughlin, M. S., and Driver, D. M., "Baseline characterization of the 30 kW miniature arc jet facility mARC at NASA Ames," *32nd AIAA Aerodynamic Measurement Technology and Ground Testing Conference*, AIAA, Washington, D.C., 2016, p. 3819.
- [18] MacDonald, M. E., Philippidis, D., Ho, T., Haw, M., Hartman, J., and McGlaughlin, M., "Build-up of the second-generation 30 kW miniature arc jet (mARC II) at NASA Ames Research Center," *AIAA Aviation 2019 FORUM*, AIAA, Dallas, Texas, 2019, p. 2857.
- [19] MacDonald, M. E., Philippidis, D., Haw, M., Schickele, D., Luis, D., Hartman, J., and McGlaughlin, M., "Initial Characterization of the 30 kW Miniature Arc Jet (mARC II) at NASA Ames Research Center," *AIAA AVIATION 2020 FORUM*, AIAA, 2020, p. 3108.
- [20] Luís, D., and MacDonald, M. E., "Emission spectroscopy characterization of electrode species in the freestream flow at the NASA Ames miniature Arc Jet II facility," *Journal of Quantitative Spectroscopy and Radiative Transfer*, Vol. 272, No. 107752, 2021.
- [21] MacDonald, M. E., Haw, M. A., Martinez, R., Colom, S., Rodrigues, J., Chung, R., and Hartman, J., "Characterizing Heat Flux in the miniature Arc jet Research Chamber (mARC II)," *AIAA AVIATION 2023 FORUM*, AIAA, San Diego, California, 2023, p. 3298.
- [22] Haw, M. A., MacDonald, M. E., and Colom, S. V., "Big-data Efficient and Automated Science Transfer (BEAST): an open-source software architecture for arc jet data management, modeling, and automation," *AIAA SCITECH 2023 Forum*, AIAA, National Harbor, Maryland, 2023, p. 2712.
- [23] ASTM International, *Standard Practice for Measuring Plasma Arc Gas Enthalpy by Energy Balance [ASTM E341-08]*, 2020.
- [24] Hightower, T. M., Balboni, J. A., MacDonald, C. L., Anderson, K. F., and Martinez, E. R., "Enthalpy by energy balance for aerodynamic heating facility at NASA Ames Research Center Arc Jet Complex," *48th International Instrumentation Symposium*, ISA, San Diego, California, 2002, pp. 1–13.
- [25] Thompson, C., Prabhu, D., Terrazas-Salinas, I., and Mach, J., "Bulk Enthalpy Calculations in the Arc Jet Facility at NASA ARC," *42nd AIAA Thermophysics Conference*, AIAA, Honolulu, Hawaii, 2011, p. 3475.
- [26] Winovich, W., *On the equilibrium sonic-flow method for evaluating electric-arc air-heater performance (NASA TN D-2132)*, 1964.
- [27] Shepard, C., Milos, F., and Taunk, J., "A sonic flow equation for electric arc jets," *24th Plasma Dynamics, and Lasers Conference*, AIAA, Orlando, Florida, 1993, p. 3183.
- [28] Wright, M. J., White, T., and Mangini, N., *Data Parallel Line Relaxation (DPLR) Code User Manual Acadia-Version 4.01.1*, 2009.
- [29] Gordon, S., and McBride, B. J., "Computer Program for Calculation Complex Chemical Equilibrium Compositions and Applications," *NASA Reference Publication 1311*, 1996.
- [30] Park, C., *Nonequilibrium Hypersonic Aerothermodynamics*, Wiley, 1990.
- [31] Park, C., "Review of chemical-kinetic problems of future NASA missions. I - Earth entries," *Journal of Thermophysics and Heat Transfer*, Vol. 7, No. 3, 1993, pp. 385–398.